Spectrochimica Acta Part B: Atomic Spectroscopy 177 (2021) 106110

Contents lists available at ScienceDirect

Spectrochimica Acta Part B: Atomic Spectroscopy

journal homepage: www.elsevier.com/locate/sab

Characterization of the ultrafine and fine particles formed during laser cladding with the Inconel 718 metal powder by means of X-ray spectroscopic techniques

Szilvia Kugler [a,b,*], Attila Nagy [a], János Osán [b], László Péter [a], Veronika Groma [b], Simone Pollastri [c], Aladár Czitrovszky [a]

[a] Wigner Research Centre for Physics, POB 49, H-1525 Budapest, Hungary
[b] Centre for Energy Research, POB 49, H-1525, Budapest, Hungary
[c] Elettra Sincrotrone Trieste, Strada Statale 14 - km 163,5, I-34149 Basovizza, Trieste, Italy

ARTICLE INFO

Keywords:
Directed energy deposition
Inconel 718
Ultrafine particles
X-ray analysis
Elemental composition
Oxidation state

ABSTRACT

Additive manufacturing is a rapidly growing industrial technology. Still, there is a lack of knowledge regarding the fine particle emission and new particle formation during the processes and their consequences on the performance of the operation and the operator's health as well. Therefore, we studied the properties of the emitted particles during the 3D printing process using the Inconel 718 (Ni-based) superalloy. The number and the mass concentrations were measured with a Scanning Mobility Particle Counter and Sizer. Size-fractionated samples were collected by a cascade impactor, and the elemental composition of the particles was determined by total-reflection X-ray fluorescence analysis, Scanning Electron Microscopy, Energy Dispersive Spectroscopy, and microscopic X-ray fluorescence analysis in the different size fractions. The oxidation states of the metals (Cr, Mn, Fe, Ni) in the samples were determined with the X-ray absorption near-edge structure (XANES) method. Most of the particles were found in the ultrafine region with a size below 100 nm, and the mass size distribution had the maximum at 85 nm. In the original powder, Ni was dominating with appr. 52 wt%, and the proportion of Cr was around 20 wt%, and Mn was below 1 wt%. In the released particles, the Ni content decreased to appr. 26 wt%, the Cr content increased to appr. 47 wt% and Mn increased to around 10 wt% for particles with a size between 0.07 and 10 μm. According to the XANES results, Cr, Mn and Fe were found to be oxidized significantly, whereas Ni remained in the metallic form in the total emitted aerosol containing mostly ultrafine particles. The enrichment and oxidation of metals were correlated with each other.

1. Introduction

Laser-based additive manufacturing (AM) is a set of new technologies where special machines build new parts using high-power lasers to melt metallic particles to form new objects layer by layer. The so-called 3D metal printing technology can be effectively used in the production of different parts for the aerospace, healthcare, energy, automotive, and other industries. There are many different AM techniques, like binder jetting, powder bed fusion, or directed energy deposition [1]. All of them have their advantages and disadvantages in various applications. The directed energy deposition method can be used to create a protective coating on a surface, to repair parts, or to build new objects, too [2]. In this technique, the intense laser beam locally melts the surface of the workpiece, where the metal particles are deposited, thus adding a new layer onto the previously deposited ones.

Many studies have been published about the effects of the process parameters on the macro- and microstructure of the created new objects, on their mechanical properties, porosity, surface quality, residual stress, etc. [1] [2–5]. However, a relatively small amount of information is available on the particle emissions during 3D metal printing processes. Concerning the indoor application of desktop 3D printers using, for example, polylactic acid (PLA), acrylonitrile butadiene styrene (ABS) thermoplastic, or polycarbonate (PC) feedstocks, people are aware of their ultrafine particle emission [6–8]. Nevertheless, laser-based AM machines are likely to generate airborne, nanoscale metal particles that may cause lung or cardiovascular diseases [9,10]. The health effects of

* Corresponding author at: Wigner Research Centre for Physics, POB 49, H-1525 Budapest, Hungary.
E-mail addresses: kugler.szilvia@wigner.hu, kugler.szilvia@ek-cer.hu (S. Kugler).

https://doi.org/10.1016/j.sab.2021.106110
Received 10 November 2020; Received in revised form 27 January 2021; Accepted 29 January 2021
Available online 2 February 2021

metal exposure of the lung are known to be a major concern, for example, in the case of hard metal workers [11] or welders [12,13]. New particle formation and the chemical composition of the plume were studied for welding processes (e.g., [14,15]). Furthermore, the fraction of the inhaled aerosol particles, which deposits in the lung, steeply increases with decreasing size in the ultrafine region [16]. Besides the health issues, the particle emission may influence the building process as well by absorbing and scattering a considerable amount of energy from the process [15,17–19], and may distort the results of the on-line optical measurements that aim to monitor the processes [20–22]. Therefore, it is of crucial importance to characterize the particle emission of AM processes and to explore its effects on the process itself and the health of the operators.

In the present study, we have characterized the emitted aerosol particles with respect to their dominating diameter range, morphology, elemental composition and oxidation state of selected metals (Cr, Mn, Fe and Ni) aiming to describe their enrichment/depletion and oxidation compared to the original feedstock powder. The number and volume distribution of the newly formed aerosol particles were determined by scanning mobility particle counter and sizer (SMPS). Simultaneously, total and size-fractionated aerosol samples were collected by a filter pack and a cascade impactor, respectively. Morphology and elemental composition of the particles were investigated by scanning electron microscopy (SEM) and energy dispersive spectroscopy (EDS). Collective elemental analysis of the aerosol particles was performed by total-reflection and microscopic X-ray fluorescence methods (TXRF, μXRF). The oxidation state of selected metals in the aerosol particles were studied non-destructively using X-ray absorption near-edge structure method (XANES). The importance of the present study is that AM machines can generate hazardous particles which can raise occupational health issues for the operators of the machines. Furthermore, the nanoparticles can influence the efficiency of the laser during operation. We used an open-table additive manufacturing machine for the experiments based on the directed energy deposition method, and the Inconel 718 nickel-based superalloy as feedstock powder.

2. Materials and methods

2.1. The additive manufacturing machine

We used the LRS EVO-Diodeline 450 based open table additive manufacturing machine from the O.R. Lasertechnologie GmbH (Dieburg, Germany) [23]. Table 1 summarizes the main features of the system.

The applied additive manufacturing machine consists of a fiber laser which emits infrared radiation at 1070 nm, a powder nozzle that delivers the shielding gas and the metallic powder to the workpiece, a four-axis motorized stage to move the piece along pre-programmed trajectories, a powder feeder, and the controller unit connected to a computer.

The laser source is a single-mode randomly polarized diode-pumped Ytterbium YLM fiber laser (IPG Photonics, Oxford, USA) with 450 W maximum mean output power. The laser power at the surface of the workpiece is controllable between 10 and 100%. Although the fiber laser can operate in pulsed mode, we used it only in continuous wave mode in our experiments. While the beam diameter of the YLM fiber laser can be as small as 50 μm in the focal plane, the spot size on the surface of the sample is adjustable from 0.48 to 3 mm, with the help of a lens of 200 mm focal length, by a motorized beam expander. A low-power visible diode laser marks the position of the infrared laser. In the experiments, the laser's measured output power was 361 W, and the spot diameter was 1.04 mm.

Table 1
Technical data of the LRS EVO-Diodeline 450 laser welding machine.

Laser type	Diode-pumped Ytterbium (Yb) Fiber Laser
Wavelength	1070 nm
Max. mean power (CW)	450 W
Max. pulse energy	45 J
Pulse peak power	4.5 kW
Pulse duration	0.5–50 ms
Pulse frequency	0.1–100 Hz
Focus diameter	0.05–2.0 mm
Operating mode	continuous wave or pulsed
Shielding/carrier gas	argon

The powder nozzle developed and manufactured by OR Laser (Dieburg, Germany), in collaboration with the Fraunhofer Institute (Munich, Germany), is in a coaxial configuration with the laser beam, and it is mounted in a fixed vertical position. The nozzle for introducing the shielding gas is in the powder nozzle after the glass window that protects the focusing lens from contamination.

A GTV PF2/1 LC powder feeder with a 3.5 × 0.3 mm^2 disk groove and argon as the carrier gas fed the system with metal powder. We set the powder focal plane to the surface of the substrate with a working distance of 7 mm. The nominal mass flow rate of the metal powder delivered by the powder feeder was 5.3 g/min. The measured carrier gas flow rate was 3.8 L/min, and the shielding argon flow rate was 10 L/min (at atmospheric pressure and room temperature). The substrate material was a rolled 304L stainless steel plate with 10 mm thickness and a 100 × 100 mm^2 surface.

The substrate with the workpiece was moved along the pre-programmed trajectory under the powder nozzle using a 3D motorized stage with a scan rate of 10 mm/s.

The device is controlled by a microcomputer, which monitors and controls the laser functions, the movements of the motorized stage, and the powder feeder. With the ORLAS SUITE application, one can design simple geometric shapes or import 3D objects created with a CAD software. After setting the laser and the trajectory parameters, it generates G-code defining 2D and 3D processing paths in three or four axes. The software transfers the G-code to the microcomputer, and the system starts building the new part. Fig. 1 shows the schematic diagram of the LRS EVO-Diodeline 450 laser welding machine equipped with the powder nozzle and the powder feeder. While many industrial grade additive manufacturing machines (3D metal printers) arrive fully enclosed to the customers, open table systems provide more flexibility to researchers, university laboratories, small/medium sized enterprises or system integrators.

2.2. Feedstock powder and substrate

Superalloys are the workhorse material in the aerospace, petrochemical, and nuclear industries where creep, corrosion, and heat resistance are needed. Inconel 718 is a nickel-based superalloy. It is a high-rupturing-strength material which offers toughness, corrosion

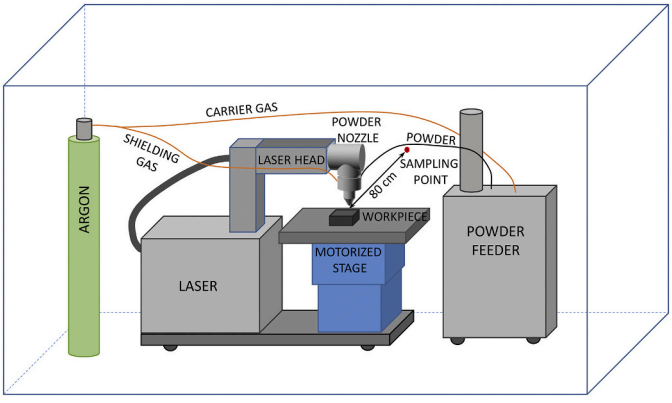

Fig. 1. Schematic diagram of the LRS EVO-Diodeline 450 based open table additive manufacturing machine.

resistance at elevated temperatures, and possesses outstanding weldability [24,25]. It can be used in a wide temperature range from −204 to 704 °C [26]. Table 2 shows the composition of Inconel 718.

In our experiments, we used the MetcoAdd 718G alloy from Oerlikon. This metal powder has a size range from 45 to 90 μm, a spherical form, and produced by the gas atomization manufacturing process.

Table 3 shows the composition of 304L stainless steel, which was used as the substrate to build demo rectangles on it. It is important to highlight the Ni, Cr and Mn content of the 304L.

2.3. Description of the experiments

The experiments took place in a small closed room of 26 m^3, where no extraction device was in operation during the measurements. The LRS EVO-Diodeline 450 based additive manufacturing machine was used to build demo rectangles of 15 × 15 × 5 mm^3 (width × length × height) on a 304L stainless steel substrate (for details, see Sections 2.1 and 2.2). The production time of one rectangle was approximately 16 min. The powder feeder fed the machine with the MetcoAdd 718G metal powder. The released particles spread in the room, mainly by Brownian diffusion, which was locally influenced by thermally generated flows around the hot metal. There was no ventilation in operation except the fans of the laser machine below the motorized table where the workpiece was built.

An SMPS (for details, see Section 2.4) was used to measure the number concentration of the released aerosol particles. The SMPS's sampling point was 15 cm from the wall of the room and 80 cm from the aerosol source. The length of the sampling line was 90 cm, and the residence time of the particles in the sampling tube was 5 s.

During the building process, size-fractionated aerosol samples were also collected on 20 × 20 mm^2 Si wafers and adhesive carbon substrates with a 9-stage May-type cascade impactor (for details, see Section 2.5) for 10 and 40 min sampling time for further morphological and chemical analysis.

Furthermore, we used Teflon membrane filters (47 mm diameter and 1 μm pore-size) to sample the total suspended particles to determine their elemental composition and oxidation state of the selected metals. Two samples were taken with 40 and 90 min sampling time and with a flow rate of 16.7 L/min.

2.4. Scanning mobility particle counter and sizer

While the diameter of the MetcoAdd 718G grains is between 45 and 90 μm, the 3D printing process forms particles dissimilar in size to the original ones, falling mainly in the ultrafine size range (below 100 nm). We used a scanning mobility particle sizer (SMPS) to measure the size distribution and the concentration of these particles. The Model 5416 SMPS+C system, which was manufactured by the Grimm Aerosoltechnik Ltd. (Ainring, Germany), uses a Vienna-type differential mobility analyzer (DMA) [27] to classify particles according to their mobility diameter, and a condensation particle counter (CPC) as a detector to count them in each size bin. The size range, which is covered by this instrument, spans from 10 to 1094 nm. The aerosol sample flow rate is 0.3 L/min, and the sheath air flow rate is 3 L/min. The CPC uses n-butanol as a working fluid and can measure concentrations up to 1.5 × 10^5 particles/cm^3 in single count mode and 10^7 particles/cm^3 in photometric mode. The size resolution of the instrument is 64 channels per decade in scanning mode. The size distribution is determined by scanning the DMA voltage and counting the particles with the CPC in each size bin. The length of one scan was 4 min, which means that faster processes may distort the measured size distribution.

The instrument's native output data is the number size distribution based on the electrical mobility diameter. Its software calculates the surface, volume, and mass size distributions from the number concentrations in each size bin. Some assumptions apply for the calculations like the particles are homogenous and spherical, and the user provides the average density value.

Table 2
Nominal composition of Inconel 718 [59].

	Inconel 718	
Element	Minimum wt%	Maximum wt%
Nickel (Ni)	50	55
Chromium (Cr)	17	21
Iron (Fe)	balance	
Niobium (Nb)	4.75	5.5
Molybdenum (Mo)	2.8	3.3
Titanium (Ti)	0.65	1.15
Cobalt (Co)	N/A	1
Aluminum (Al)	0.2	0.8
Manganese (Mn)	N/A	0.35
Silicon (Si)	N/A	0.35
Copper (Cu)	N/A	0.3
Carbon (C)	N/A	0.08
Phosphorus (P)	N/A	0.015
Sulfur (S)	N/A	0.015
Boron (B)	N/A	0.006

Table 3
Composition of 304L stainless steel.

	304L	
Element	Minimum wt%	Maximum wt%
Nickel (Ni)	8	12
Chromium (Cr)	18	20
Aluminum (Al)	N/A	0.1
Carbon (C)	N/A	0.03
Manganese (Mn)	N/A	2
Silicon (Si)	N/A	0.75
Phosphorus (P)	N/A	0.045
Sulfur (S)	N/A	0.03

2.5. Cascade impactor sampling

New particles form from the metal vapor above the high-temperature melt pool with a size mainly below 100 nm during the building of new objects with the AM machine. Size-fractioned aerosol sampling was performed with a 9-stage in-house developed extension of the May-type cascade impactor [28] to be able to study the chemical and morphological composition of particles not only in the fine but also in the ultrafine size fraction (Fig. 2). Cascade impactors separate the aerosol particles based on their inertia by increasing the speed of the airflow by means of jet nozzles. Particles that cannot follow the airstream are collected on plates via impaction (see Fig. 2). The area of the nozzles decreases stage by stage, hence allowing the collection of particles of consecutively decreasing diameters. The May-impactor has aerodynamic cut-off diameters of 17.9, 8.9, 4.5, 2.25, 1.13, 0.57, 0.29, 0.18, and 0.07 μm, for stages 1 to 9, respectively, at a flow rate of 16.7 L/min. Samples were collected on 20 × 20 mm^2 Si wafers at stages 3 to 9 and on adhesive carbon substrates at all stages except stage 1. The deposition pattern of aerosol particles is a thin stripe with a 50 mm length and widths decreasing with increasing stage number from 0.1 mm (stage 9) to 1.8 mm (stage 2). Because of the high concentrations measured in the laboratory during the AM process, the sampling time was short, 10 min for Si substrates, and 40 min for carbon substrates. It should be noted that the cascade impactor separates particles based on the aerodynamic diameter that can differ from the electrical mobility diameter based on the shape and density of the particles [29].

2.6. Total-reflection X-ray fluorescence analysis

The elemental composition of size-fractionated aerosol samples collected on Si substrates was determined by total-reflection X-ray fluorescence analysis (TXRF). A compact laboratory TXRF system [30]

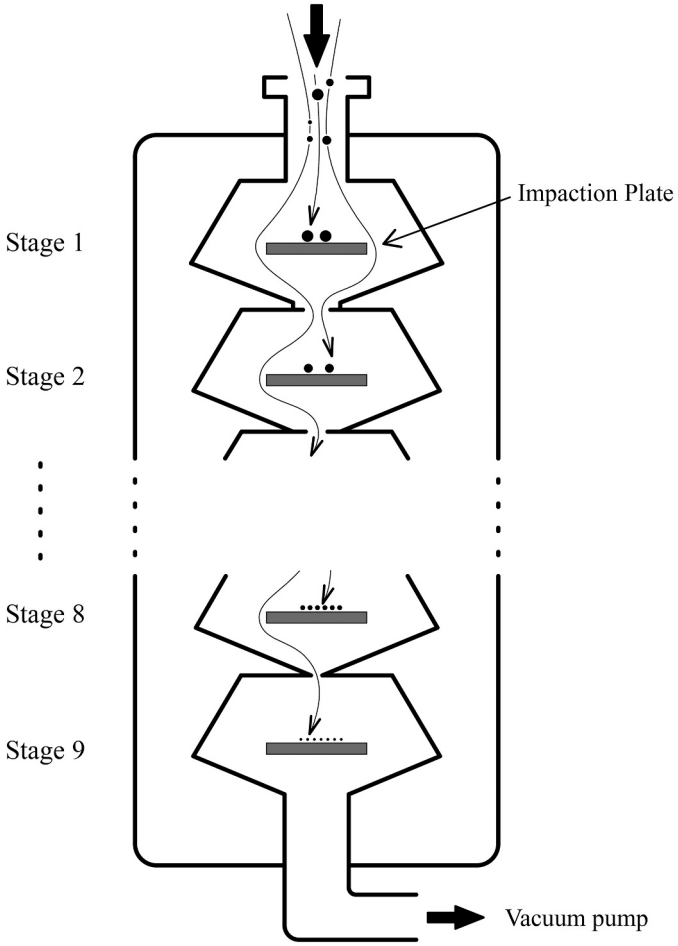

Fig. 2. Schematic diagram of the May-type cascade impactor.

was applied for the present study. A 50-W microfocus Mo-anode X-ray tube (Petrick, Bad Blankenburg, Germany) was operated at 50 kV and 1 mA, and Mo-Kα X-rays were selected for excitation using a Mo/Si multilayer monochromator (AXO, Dresden, Germany). Si wafer squares were analyzed with aerosol deposit stripes horizontally, perpendicular to the beam direction. X-ray spectra were recorded using a 7 mm^2 silicon drift detector (KETEK, Munich, Germany) with a round Zr collimator and an analog signal processing unit (PGT, Princeton, USA). Measurements were performed in air. Counting time was set to 1600 s for stage 9 and 3000 s for the remaining stages. The AXIL software [31] was used to evaluate X-ray spectra. Since aerosol particles are deposited as a stripe, the usual internal standardization is not straightforward; thus, the quantification of elemental content was performed using calibration based on external standards (Merck IV, 23 elements). The elemental concentrations were calculated for each size fraction considering the total length of deposited stripes (50 mm for each impactor stage) and the collected air volume. Detection limits of 100 pg/m^3 at each impactor stage were reached using the system for transition metals in ambient aerosol particles [32], assuring a reliable determination of elemental size distributions in the present study.

2.7. Scanning electron microscope and Energy Dispersive Spectroscopy

The size-fractionated samples on the impactor plates were analyzed by a scanning electron microscope (SEM) to determine the morphology and composition of the particles. We used a Tescan MIRA3 scanning electron microscope for this study. We analyzed the elemental composition of the particles with Energy Dispersive Spectroscopy (EDS) produced by EDAX Inc. and used the APEX™ Software for EDS for data processing. Secondary electron images were recorded for studying the particle morphology. The EDS analysis proved to be reliable by using an acceleration voltage of 20 kV.

2.8. Microscopic X-ray fluorescence analysis

Measurements of the original feedstock powder and the collected aerosol particles were performed on an in-house developed laboratory μXRF setup [33], allowing point analysis and recording of 2D elemental maps. Since the X-ray source cannot be moved, scanning is performed through the movement of the sample across a stationary X-ray microbeam. A low-power rhodium-anode X-ray source (iMOXS, IfG, Berlin, Germany) [34] coupled with a polycapillary minilens (IfG, Berlin, Germany) was used to form a 20 μm microbeam [35]. Between the X-ray tube and the polycapillary, a 25-μm Rh beam filter was used in order to enhance Rh K characteristic lines in the excitation spectrum. In order to detect the emitted characteristic X-rays, a Peltier-cooled Si drift detector (SDD) with an active area of 30 mm^2 (KETEK, Munich, Germany) was used. The measurement process is computer-controlled by an in-house developed LabView-based software specifically designed for the system [33]. It controls the sample stage, the spectrum acquisition process, and displays the optical image of the sample.

2D elemental maps were recorded using a 10 μm step-size, and 3 s dwell time per pixel on individual grains of the original metallic feedstock powder. X-ray spectra were collected in the center positions of individual grains, for 600 s. Longer measurement time was necessary for the deposited aerosol particles. The recorded X-ray spectra were evaluated by the AXIL software [31]. The system was calibrated using metallic foils in the range of titanium to molybdenum.

2.9. X-ray absorption near-edge structure

In order to determine the oxidation state of selected metals in the total and size-fractionated (stages 9 and 8) aerosol samples, X-ray absorption near-edge structure (XANES) spectra were collected at the Elettra synchrotron radiation facility (Trieste, Italy). Measurements were performed at the K absorption edges of Cr, Mn, Fe, and Ni, both at the XAFS [36] and the XRF [37,38] beamlines.

Spectra were collected using Si (111) monochromator in both beamlines. At the XRF beamline, the monochromator was calibrated before the measurements and spectra from size-fractionated aerosol particles deposited on Si wafers were measured in TXRF geometry, using an XFlash 5030 SDD (Bruker, Berlin, Germany).

At the XAFS beamline, the energy calibration was accomplished by collecting simultaneously a reference metal foil placed in a second experimental chamber after the sample and after the I_1 ionization chamber. In this case, the geometry for fluorescence mode measurements on filter samples was standard 45°/45°, using an AXAS-M SDD (KETEK GmbH, Munich, Germany) detector. XANES spectra were collected also in transmission mode (sample at 90° with respect to the beam) on pure Cr, Mn, Fe and Ni metallic foils, stainless steel foils (301 and 316L) and reference compounds (Cr_2O_3, Fe_2O_3 and NiO) in the form of pressed pellets. Stainless steel foils contain 16–19 wt% Cr, 6.0–13 wt % Ni and 65–75 wt% Fe.

All spectra were collected at room temperature both in air (XAFS beamline) and in high vacuum (XRF beamline) conditions, using a variable energy step as a function of the energy: Large step (5 eV) in the first 200 eV of the spectrum, smaller step (0.2 eV) in the near-edge region and a *k*-constant step of 0.03 $Å^{-1}$ (up to 1.8 eV) further above the absorption edge. The time per step was 5 s for fluorescence and 2 s for transmission mode measurements.

For each sample, multiple spectra have been collected and merged in order to increase the signal to noise ratio. The oxidation state of metals in the aerosol samples was determined using least-squares Linear Combination Fitting (LCF) based on reference spectra collected for model compounds of known oxidation state. Background removal,

normalization of XANES spectra as well as LCF were performed using the Athena software package [39].

3. Results

3.1. Number and mass concentrations of the aerosol particles released during laser cladding with metal powder

The SMPS (for details see Section 2.4) was detecting the number size distribution of the newly formed aerosol particles using 4 min sampling time with downward scanning mode. The results are shown in Fig. 3, together with the calculated volume size distribution assuming spherical particles.

Based on the measured data, the vast majority of the formed particles are below 100 nm, and more than 70% of the corresponding volume or mass falls below 100 nm. The peak of the number size distribution is at 53 nm, the total concentration is 9.3×10^5 particles/cm^3, and the mode of the volume size distribution is at 85 nm (Table 4). We have to note here that the particle concentration above the melt pool was beyond the limit of the SMPS (10^7 particles/cm^3). For the representative sampling above the melt pool, we placed the probe to a 15 mm distance from the source of the particles. Considering the high concentrations, the size distribution of the particles near the melt pool is definitely different from the one measured at 80 cm distance, i.e. particles are smaller and the number concentration is higher.

3.2. Elemental mass concentrations in the aerosol released during laser cladding with metal powder

SEM (for details see Section 2.7) was applied to determine the morphology and the size distribution of the original MetcoAdd 718G powder. Fig. 4 shows a typical SEM image for particles weakly attached to an adhesive carbon tape. The measured size values agreed well with the specifications of the feedstock powder, and most of the grains had a spherical, and some of them had an elongated form. As a result of the gas atomization manufacturing process, one can observe smaller satellite grains stuck to the larger spherules with the size of a couple of microns.

The elemental composition of the original MetcoAdd 718G powder was determined with SEM/EDS and also using the μXRF technique (for details see Sections 2.7 and 2.8). Fig. 5 shows the results of the two different methods. The three most dominating elements are Ni appr. 52 wt%, Cr 20 wt%, and the Fe 18 wt%. The detected composition agrees well with the nominal elemental composition of the Inconel 718 superalloy (see Table 2).

Two samples were collected on Teflon membrane filters for the whole size range of the particles [40] and were analyzed with the μXRF technique. Fig. 6 shows the elemental composition of the sampled particles.

Fig. 6 presents a different elemental ratio compared to the feedstock material. The newly formed particles contain 42% of Cr, 29% of Ni, and 18% of Fe, which is significantly different from the original material.

The measured morphology of the newly formed aerosol is shown in Fig. 7. In the figure one can observe primary spherical particles with a size in the order of 10 nm, and aggregates formed by these small

Table 4
Statistical data of the size distribution based on SMPS measurements.

	Mean (nm)	Mode (nm)	Median (nm)	Geometric standard deviation	Total
Number	42.44	53.28	43.42	1.68	930,000 (1/cm^3)
Volume	89.74	85.05	81.92	1.86	110.30 (μm^3/cm^3)

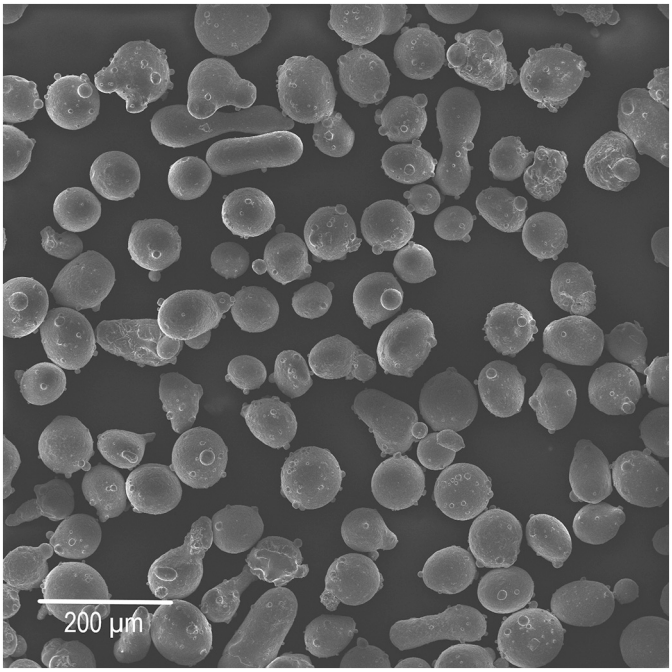

Fig. 4. Secondary electron image of the MetcoAdd 718G grains.

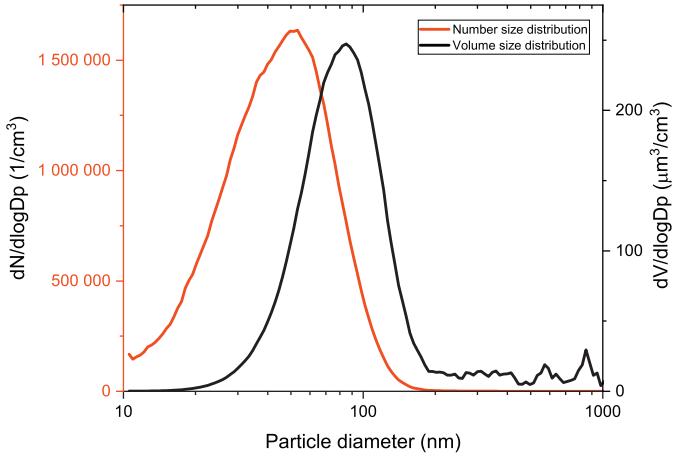

Fig. 3. Number and volume size distributions during cladding with powder measured in the fine fraction (below 1 μm).

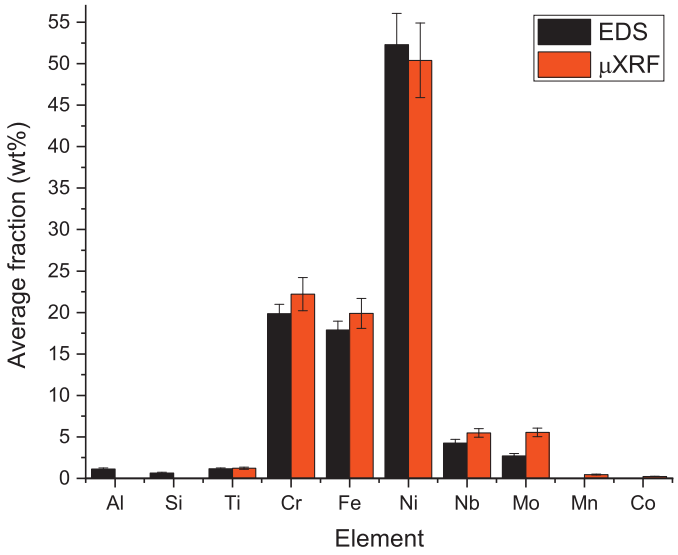

Fig. 5. Elemental composition of the original MetcoAdd 718G powder determined by SEM/EDS and μXRF. The error bars are the calculated standard deviation values of 3 measurements.

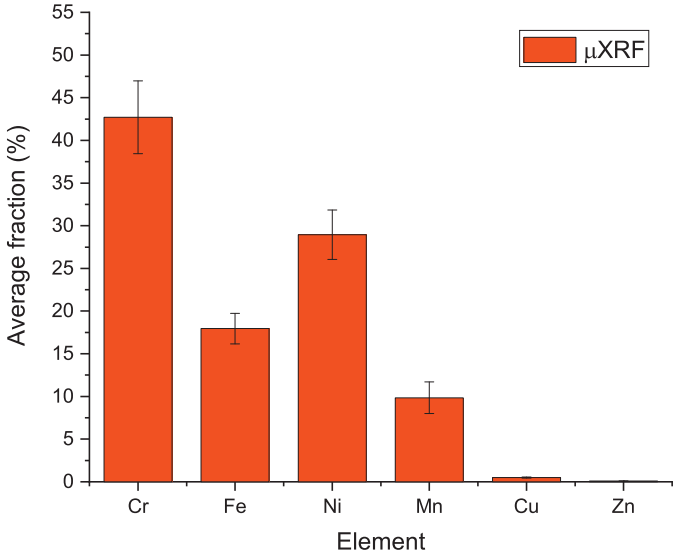

Fig. 6. Elemental composition of the aerosol particles released during the intensive laser-matter interaction (samples collected on Teflon membrane filters).

particles. These aggregates have similar morphology to soot [41] and flame-generated zirconia [42] aggregates. There are also self-standing particles on the impactor plate with a diameter much below the size range to which the impactor stage was rated. These particles are likely to be formed as the debris of the larger ones that disintegrated upon the collision with the impactor plate. Hence, the impacting conditions and the diameter of the particles later observed on the collection substrate surface cannot be correlated.

Table 5 shows the measured mass concentrations of the selected elements in the different size fractions in terms of aerodynamic diameter using the total-reflection X-ray fluorescence method.

The TXRF analysis shows that 92% of the particles were between 70 and 180 nm in the size range covered by the cascade impactor, and the mass concentration on this stage was 66.0 μg/m^3. Based on calculations provided for soot aggregates [41], the effective density was found to be 0.19 (uncompacted soot) to 0.30 (compacted soot) times the nominal bulk density. Considering the nominal density of Inconel 718 alloy as 8.2 g/cm^3, the effective density of the aggregates can be estimated as 1.6–2.5 g/cm^3 supporting that the majority of particles of 85 nm mass median mobility diameter (see Fig. 3 and Table 4) are collected on the smallest size class. The total mass concentration was 71.7 μg/m^3 in the whole covered size range (between 0.07 and 10 μm). The Ni-to-Cr ratio changed from approximately 2 (original metal powder) to around 0.67 (new aerosol particles). 95% of the Cr and 89% of the Ni was in particles between 70 and 180 nm. The Mn content was below 1 wt% in the original powder, we measured 10 wt% for the particles of diameter between 70 and 180 nm in the released aerosol.

Fig. 8 shows the mass concentration of the elements measured with different detection techniques between 70 and 180 nm size range. Both methods show quite similar results. The oxygen is detected only with SEM/EDS since the TXRF method was not performed under vacuum conditions.

3.3. Oxidation state of metals by XANES

Cr, Mn, Fe and Ni K-edge XANES spectra collected for aerosol

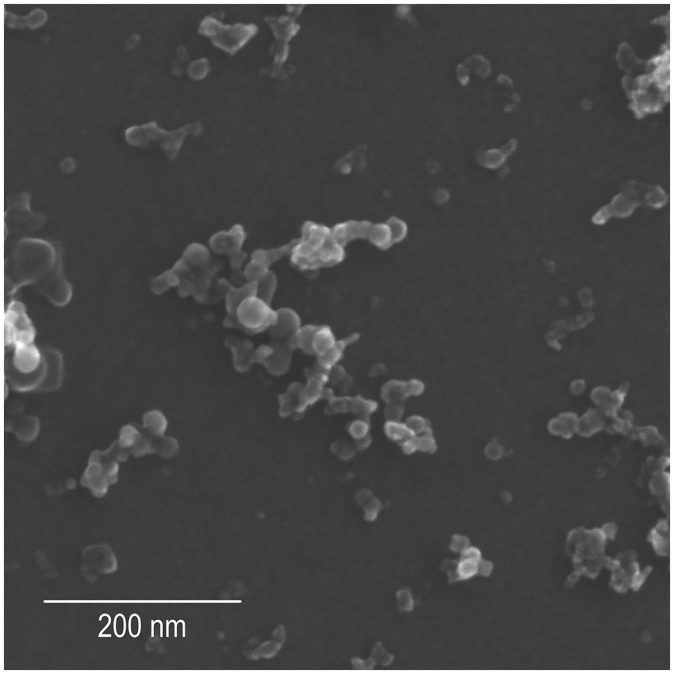

Fig. 7. Secondary electron image of the MetcoAdd 718G particles collected for the size range from 70 to 180 nm Si wafers.

Table 5
Elemental mass concentrations in the aerosol released during laser cladding with the MetcoAdd 718G metal powder.

Mass concentration (μg/m^3)				
Element	70–180 nm	180–300 nm	0.3–10 μm	Total 0.07–10 μm
Ni	17.30	0.40	1.60	19.30
Cr	29.00	0.60	1.00	30.60
Fe	11.90	0.30	0.70	12.90
Mn	6.90	0.10	0.10	7.10
S	0.15	0.10	0.49	0.74
Cu	0.27	0.01	0.02	0.30
Zn	0.03	0.00	0.00	0.03
Other	0.44	0.00	0.24	0.68
Total	66.0	1.5	4.2	71.7

particles and metals (stainless steel) are summarized in Fig. 9. In order to compare the spectra collected around K-edges of different metals, the energy scale is displayed as relative to the respective K-edges (i.e. 5989 eV for Cr, 6539 eV for Mn, 7112 eV for Fe and 8333 eV for Ni). The oxidation state can be derived from the chemical shift of the absorption edge towards positive energies for oxidized chemical forms. Peaks and oscillations near the absorption edges can also be used as fingerprints for specific chemical states, e.g. a specific sharp and narrow peak at 4.4 eV relative energy is characteristic for Cr^{6+} compounds [43].

In general, XANES spectra of total aerosol on filter (XAFS beamline), 70–180 nm and 180–300 nm fractions (XRF beamline) look similar for all selected metals. Because of the structural difference between pure metals and alloys, [44–46] oscillations with smaller amplitude are observed in the XANES spectra of metals in alloys. For this reason, Cr, Fe and Ni K-edge XANES spectra collected on stainless steel 301 (containing around 16–19 wt% Cr and 6–9 wt% Ni) were used for comparison and further evaluation.

Since the edge features (at around 0 eV relative) are smaller with respect to the metallic spectra for Cr, Mn and Fe, the presence of oxidized metals is significant in the aerosol samples (see Fig. 9). For Mn, only a small step is visible at the nominal absorption edge energy of Mn metal (0 eV relative), indicating that Mn is highly oxidized. For Cr, the presence of Cr^{6+} could be excluded due to the absence of characteristic pre-edge peak.

Quantitative information on the oxidation state of Cr, Mn, Fe and Ni was obtained by LCF performed using the standard spectra for Cr, Fe and Ni in stainless steel (301), Mn metal and reference compounds of higher oxidation states like $Cr^{3+}$and Cr^{6+}, Mn^{2+} and Mn^{3+}, Fe^{2+} and Fe^{3+} as well as Ni^{2+}. The fitting results are summarized in Table 6.

Among the four studied metals, Cr, Mn and Fe were found to be oxidized significantly, whereas Ni remained in the metallic form in the total aerosol. The order of metals based on oxidation degree was found as Mn > Cr > Fe > Ni (see Table 6). Size-fractionated samples in the 70–180 nm and 180–300 nm diameter range contained metallic Cr and Fe at the 79% and 77% level, respectively, significantly higher than in the total aerosol samples. Taking into account the SMPS results as well, the total aerosol collected by the filter is dominated by ultrafine particles representing more than 70% of the total mass (see Fig. 3). It means that the ultrafine aerosol particles contain the highest fraction of oxidized Mn, Cr and Fe, so oxidation occurs despite the presence of the shielding gas.

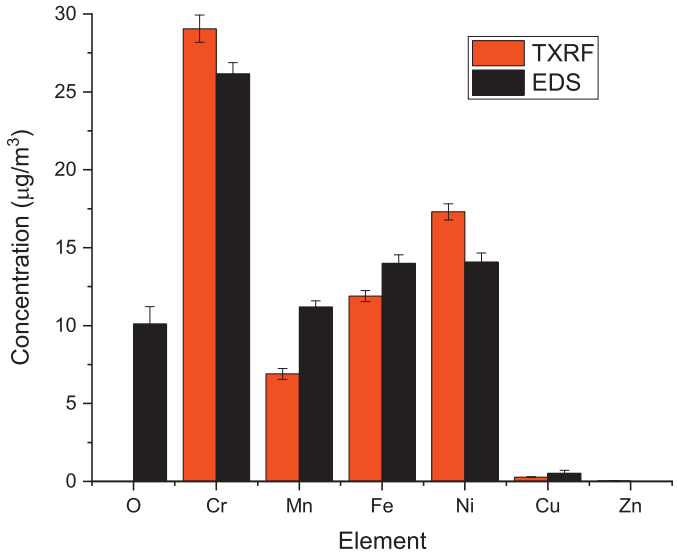

Fig. 8. Mass concentrations of the elements in size range from 70 to 180 nm measured with TXRF and SEM/EDS.

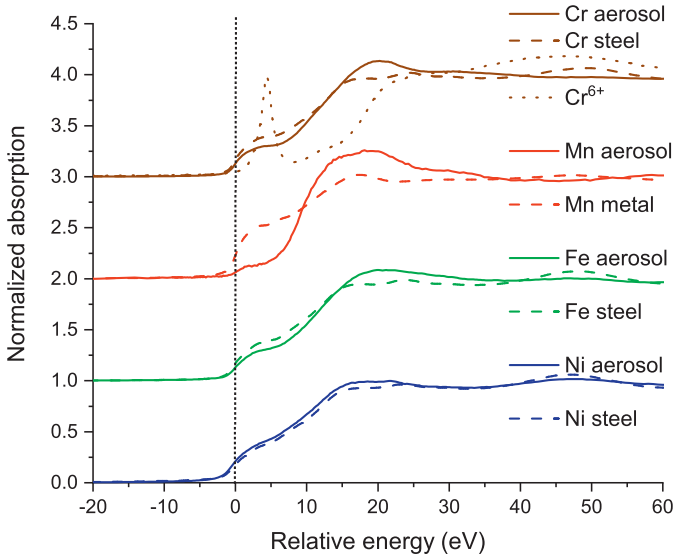

Fig. 9. Comparison of Cr, Mn, Fe and Ni normalized XANES spectra of total aerosol collected on filter and metals.

Table 6
LCF results for Cr, Mn, Fe and Ni K-edge XANES of aerosol particles, using reference spectra of known oxidation states.

Sample	Total aerosol on filter (mostly ultrafine particles)	70–180 nm fraction	180–300 nm fraction
Cr^0 fraction	0.67 ± 0.01	0.79 ± 0.01	0.79 ± 0.05
Cr^{3+} fraction	0.33 ± 0.02	0.21 ± 0.03	0.21 ± 0.03
Cr^{6+} fraction	–	–	–
Cr mean oxidation number	**+0.97 ± 0.05**	**+0.63 ± 0.10**	**+0.64 ± 0.10**
Mn^0 fraction	0.10 ± 0.02	n.a.	n.a.
Mn^{2+} fraction	0.44 ± 0.02	n.a.	n.a.
Mn^{3+} fraction	0.46 ± 0.02	n.a.	n.a.
Mn mean oxidation number	**+2.26 ± 0.10**	**n.a.**	**n.a.**
Fe^0 fraction	0.74 ± 0.01	0.77 ± 0.01	0.77 ± 0.01
Fe^{2+} fraction	0.04 ± 0.01	0.10 ± 0.01	0.12 ± 0.01
Fe^{3+} fraction	0.22 ± 0.01	0.13 ± 0.01	0.11 ± 0.01
Fe mean oxidation number	**+0.73 ± 0.02**	**+0.59 ± 0.05**	**+0.57 ± 0.05**
Ni^0 fraction	0.96 ± 0.01	0.93 ± 0.01	0.93 ± 0.01
Ni^{2+} fraction	0.04 ± 0.01	0.07 ± 0.01	0.07 ± 0.01
Ni mean oxidation number	**+0.08 ± 0.02**	**+0.14 ± 0.02**	**+0.14 ± 0.02**

4. Discussion

During the intense laser–metal interaction in the studied additive manufacturing process, the evaporated atoms of the metallic parts mix with the ambient gas, and the subsequent expansion of this mixture leads to its cooling and supersaturation. As a result, new particles form by nucleation and subsequent growth of the condensed-phase clusters becomes possible.

4.1. Elemental composition and oxidation states of selected metals in the emitted particles

The possible explanation for the enrichment of metals in the aerosol compared to the original feedstock powder is that Cr has one order of magnitude higher, and Mn has five orders of magnitudes higher vapor pressure than Ni at 1200 °C temperature. As the intense laser beam melts the workpiece and the metal particles, first the Mn, then Cr and at last Ni evaporate, the newly formed ultrafine particles contain Mn and Cr in higher concentrations accordingly than in the original material. The high apparent enrichment ratio makes it necessary to look for a secondary source of the Mn besides the feedstock powder. One should note that the substrate material contains Fe, Cr and small amount of Mn, that can also play a role in enrichment when the first layer is built during the AM process. The origin of the Mn can be the feedstock or the substrate 304L as well. The Inconel 718 contains only 0.35% and the substrate a maximum of 2% of Mn.

The trend of enrichment in the ultrafine aerosol fraction is the same as that of oxidation, i.e. Mn > Cr > Fe > Ni (Fig. 10). There is a hidden

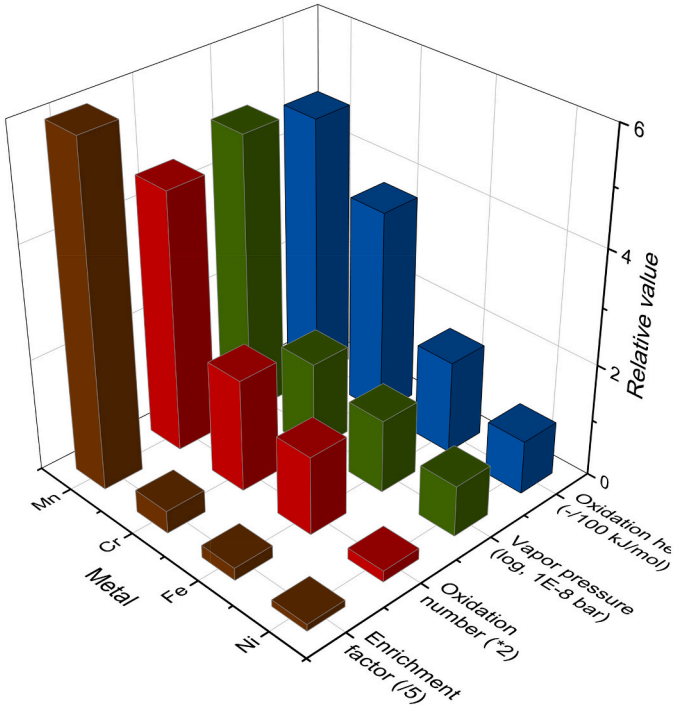

Fig. 10. Comparison of enrichment factor, mean oxidation number, volatility and oxidation heat of metals in ultrafine aerosol at 1200 °C.

causality relationship between these trends. The more volatile a component is, the more it can enrich in the re-precipitated fraction of the aerosol. And at the same time, the larger is its atomization ratio due to the volatility, which provides an effective reactivity with the surrounding gases. Oxidation is due to the effective atomization, which is the consequence of the volatility. This is an indirect evidence for that the small particles do not form by the simple removal of the excess material from large particles but an evaporation–precipitation mechanism is effective.

4.2. Occupational health effects of the released aerosol particles

The chemical composition of the released aerosol particles can be characterized by significant amounts of Fe, Cr, Mn, and Ni, where Ni, Cr, and Mn are toxic metals [47–49]. An important feature of the ultrafine metal oxide particles is the Mn enrichment, which, together with their large amount, increase their toxic potential as a function of decreasing particle size. The measured value of the Mn concentration was between 26 and 50 μg/m^3, which reaches the occupational health limit value for the respirable fraction (50 μg/m^3) of this element in the European Community [50]. Some countries, for example Germany has even a more severe limit value for this fraction, namely 20 μg/m^3.This metal can damage the central nervous system and cause neuropsychiatric disturbances [47]. According to several studies [51,52] Ni in metal form is not considered as potentially carcinogenic component. Since 96% of Ni was found in metallic form, serious health effects can be excluded from the Ni. Some European countries have regulations for the occupational exposure limit values for Ni, but there is no uniform legislation. For example, in some countries the current limit value for the inhalable fraction is 30 μg/m^3, which is exceeded by the Ni concentrations measured in the released aerosol.

Fortunately, no Cr^{6+} was detected, which is the most toxic and carcinogenic form of this metal. The total Cr concentration varied from 134 to 179 μg/m^3. The occupational health limit value for this component is 2 mg/m^3 for 8 h in the inhalable fraction [53]. Although the measured concentration is one order of magnitude lower than the limit value, one should consider that the vast majority of the released particles was found to be in the respirable fraction for which the limit values are generally stricter if available. The Ni concentrations exceeded whereas the Cr and Mn concentrations were close to or below the currently valid limit values; therefore it is highly recommended for the operators of the machine to wear suitable protective equipment and to use extraction device. There are new recommendations for the European Community to lower or set occupational health limit values for potentially toxic metal compounds in the respirable aerosol fraction [54].

4.3. Effects of the released ultrafine particles on the quality of the AM process

The power stability of the energy source is an important factor in additive manufacturing processes. The main contributions to the attenuation of the laser power that reaches the surface of the substrate in laser-based energy deposition processes are attributed to the reflection from the substrate surface and the reflection and absorption by the powder stream [55]. However, the power stability is influenced by the generated ultrafine particles as well. While, in our study, the size of the new particles was mainly below 100 nm, their measured number concentration was in the order of 10^6 particles/cm^3 at 80 cm, and above 10^7 particles/cm^3 at 15 mm distance from the particle formation. Since these nanoscale metal particles can absorb or scatter laser radiation, it affects the quality of the beam focusing and the temporal power stability of the laser radiation that reaches the surface. In the case of high power fiber laser welding it was shown that the amplitude of the fluctuations of the beam attenuation value could be higher than 10% when the beam propagates through the generated aerosol-cloud above the melt pool [18]. This effect can negatively influence the quality of the building process. In the case of laser-based powder bed fusion of pure Zn powder, the low densification of the created parts was attributed to the fluctuation of the laser energy deposited on the powder bed due to the attenuation of the laser beam by small particles inside the evaporation fume [56–58].

5. Conclusions

We characterized aerosol particles formed by vapor phase nucleation during the interaction of intense laser beam and metallic alloys in laser cladding processes. The size distribution, number and elemental mass concentrations, the size-fractionated elemental composition and oxidation state of the metallic parts of the released ultrafine aerosol particles were measured when an additive manufacturing machine was building demo objects from nickel-based metal alloy powder.

The SMPS measurements show that the majority of the particles were in the ultrafine region with a size below 100 nm, and the mass size distribution of the released particles shows a pronounced peak at 85 nm. The Ni-to-Cr ratio changed from approximately 2 (original metal powder) to around 0.67 (aerosol particles). Although the amount of Mn was around or below the detection limit in the original feedstock powder, a significant amount was released during laser cladding. 97% of Mn, 95% of Cr and 89% of Ni were in particles in 70 to180 nm size range.

The elemental compositions of the sampled aerosol particles were determined through energy dispersive spectroscopy, total-reflection and μX-ray fluorescence techniques, and the results were in good agreement.

XANES results revealed that Mn, which metal was the most enriched in the ultrafine aerosol fraction, was the most oxidized in the smallest particulate fraction. Cr was also oxidized significantly, but the presence of Cr^{6+} could be excluded. The order of metals based on formal oxidation number was found as Mn > Cr > Fe > Ni, and this order is also relevant for the volatility of these metals.

The newly formed nanoscale metallic particles are potentially toxic and/or carcinogenic to humans, which indicates the necessity of applying proper extraction devices and/or personal protection equipment.

The new metal and metal oxide particles formed during the process can cause considerable extinction of a fiber laser beam during cladding. Therefore, the metal vapor condensation effect should be taken into account and monitored during the processes.

CRediT authorship contribution statement

Szilvia Kugler: Conceptualization, Methodology, Investigation, Writing - original draft. **Attila Nagy:** Investigation, Writing - review & editing, Funding acquisition. **János Osán:** Conceptualization, Methodology, Investigation, Writing - review & editing, Funding acquisition. **László Péter:** Investigation, Writing - review & editing. **Veronika Groma:** Investigation, Writing - review & editing. **Simone Pollastri:** Investigation, Writing - review & editing. **Aladár Czitrovszky:** Writing - review & editing.

Declaration of Competing Interest

The authors declare that they have no known competing financial interests or personal relationships that could have appeared to influence the work reported in this paper.

Acknowledgements

This work was supported by the Hungarian National Research Development and Innovation Fund under grant no. 2017-1.3.1-VKE-2017-00039 and by European Structural and Investment Funds jointly financed by the European Commission and the Hungarian Government under grant no. VEKOP-2.3.2-16-2016-00011. We also acknowledge the staff of XAFS and XRF beamlines of Elettra Sincrotrone Trieste for

collecting the data during in-house beamtime.

References

[1] H. Fayazfar, et al., A critical review of powder-based additive manufacturing of ferrous alloys: process parameters, microstructure and mechanical properties, Mater. Des. 144 (Apr. 2018) 98–128, https://doi.org/10.1016/j.matdes.2018.02.018.

[2] S.M. Thompson, Z.S. Aspin, N. Shamsaei, A. Elwany, L. Bian, Additive manufacturing of heat exchangers: a case study on a multi-layered Ti-6Al-4V oscillating heat pipe, Addit. Manuf. 8 (Oct. 2015) 163–174, https://doi.org/10.1016/j.addma.2015.09.003.

[3] T. DebRoy, et al., Additive manufacturing of metallic components – process, structure and properties, in: Progress in Materials Science 92, Elsevier Ltd, 1 Mar 2018, pp. 112–224, https://doi.org/10.1016/j.pmatsci.2017.10.001.

[4] D. Herzog, V. Seyda, E. Wycisk, C. Emmelmann, Additive manufacturing of metals, Acta Mater. J. 117 (2016) 371–392, https://doi.org/10.1016/j.actamat.2016.07.019.

[5] B. Bax, R. Rajput, R. Kellet, M. Reisacher, Systematic evaluation of process parameter maps for laser cladding and directed energy deposition, Addit. Manuf. 21 (May 2018) 487–494, https://doi.org/10.1016/j.addma.2018.04.002.

[6] B. Stephens, P. Azimi, Z. El Orch, T. Ramos, Ultrafine particle emissions from desktop 3D printers, Atmos. Environ. 79 (Nov. 2013) 334–339, https://doi.org/10.1016/j.atmosenv.2013.06.050.

[7] D. Rejeski, F. Zhao, Y. Huang, Research needs and recommendations on environmental implications of additive manufacturing, in: Additive Manufacturing 19, Elsevier B.V., 1 Jan 2018, pp. 21–28, https://doi.org/10.1016/j.addma.2017.10.019.

[8] S.J. Park, et al., 3D printing of bio-based polycarbonate and its potential applications in ecofriendly indoor manufacturing, Addit. Manuf. 31 (Jan. 2020), 100974, https://doi.org/10.1016/j.addma.2019.100974.

[9] P. Andujar, et al., Role of metal oxide nanoparticles in histopathological changes observed in the lung of welders, Part. Fibre Toxicol. 11 (1) (2014) 2–13, https://doi.org/10.1186/1743-8977-11-23.

[10] S.A. Ljunggren, et al., Biomonitoring of metal exposure during additive manufacturing (3D printing), Saf. Health Work 10 (2019) 518–526, https://doi.org/10.1016/j.shaw.2019.07.006.

[11] P. Rehfisch, et al., Lung function and respiratory symptoms in hard metal workers exposed to cobalt, J. Occup. Environ. Med. 54 (4) (Apr. 2012) 409–413, https://doi.org/10.1097/JOM.0b013e31824d2d7e.

[12] S.W. Christensen, J.P. Bonde, Ø. Omland, A prospective study of decline in lung function in relation to welding emissions, J. Occup. Med. Toxicol. 3 (6) (2008) 1–8, https://doi.org/10.1186/1745-6673-3-6.

[13] M. El-Zein, J. Malo, C. Infante-Rivard, D. Gautrin, Prevalence and association of welding related systemic and respiratory symptoms in welders, Occup. Environ. Med. 60 (2003) 655–661, https://doi.org/10.1136/oem.60.9.655.

[14] N. Jenkins, T. Eagar, Sponsored by the American Welding Society and the Welding Research Council Chemical Analysis of Welding Fume Particles Airborne particle size is the most important factor in determining the accuracy of a method for chemical analysis, Weld. J. (2013) 87–93.

[15] T. Scholz, K. Dickmann, A. Ostendorf, H. Uphoff, M. Michalewicz, Effect of process parameters on the formation of laser-induced nanoparticles during material processing with continuous solid-state lasers, J. Laser Appl. 27 (3) (Aug. 2015), 032001, https://doi.org/10.2351/1.4916081.

[16] M. Hussain, P. Madl, A. Khan, Lung deposition predictions of airborne particles and the emergence of contemporary diseases Part-I, Health 2 (2) (2011) 51–59.

[17] Y. Kawahito, N. Matsumoto, M. Mizutani, S. Katayama, Characterisation of plasma induced during high power fibre laser welding of stainless steel, Sci. Technol. Weld. Join. 13 (8) (Nov. 2008) 744–748, https://doi.org/10.1179/136217108X329313.

[18] P.Y. Shcheglov, S.A. Uspenskiy, A.V. Gumenyuk, V.N. Petrovskiy, M. Rethmeier, V. M. Yermachenko, Plume attenuation of laser radiation during high power fiber laser welding, Laser Phys. Lett. 8 (6) (2011) 475–480, https://doi.org/10.1002/lapl.201110010.

[19] J. Zou, W. Yang, S. Wu, Y. He, R. Xiao, Effect of plume on weld penetration during high-power fiber laser welding, J. Laser Appl. 28 (2) (May 2016), 022003, https://doi.org/10.2351/1.4940148.

[20] D. You, X. Gao, S. Katayama, Monitoring of high-power laser welding using high-speed photographing and image processing, Mech. Syst. Signal Process. 49 (1) (2014) 39–52, https://doi.org/10.1016/j.ymssp.2013.10.024.

[21] S.K. Everton, M. Hirsch, P. Stravroulakis, R.K. Leach, A.T. Clare, Review of in-situ process monitoring and in-situ metrology for metal additive manufacturing, Mater. Des. 95 (2016) 431–445, https://doi.org/10.1016/j.matdes.2016.01.099.

[22] U.A. Taparli, L. Jacobsen, A. Griesche, K. Michalik, D. Mory, T. Kannengiesser, In situ laser-induced breakdown spectroscopy measurements of chemical compositions in stainless steels during tungsten inert gas welding, Spectrochim. Acta Part B At. Spectrosc. 139 (2018) 50–56, https://doi.org/10.1016/j.sab.2017.11.012.

[23] T. Kramár, J. Tauer, P. Vondrouš, Welding of nitinol by selected technologies, Acta Polytech. 59 (1) (Feb. 2019) 42–50, https://doi.org/10.14311/AP.2019.59.0042.

[24] M. Szustecki, L. Zrodowski, R. Sitek, R. Cygan, Microstructure and properties of IN 718 nickel-based superalloy manufactured by means of selective laser melting, Adv. Appl. Plasma Sci. 11 (September) (2017) 3–7.

[25] S. Luo, W. Huang, H. Yang, J. Yang, Z. Wang, X. Zeng, Microstructural evolution and corrosion behaviors of Inconel 718 alloy produced by selective laser melting following different heat treatments, Addit. Manuf. 30 (Dec 2019), https://doi.org/10.1016/j.addma.2019.100875.

[26] P.D.I. Torino, Characterization of Inconel 718 Fabricated by Selective Laser Melting (SLM) to Achieve more Productive Parameters, 2019.

[27] W. Winklmayr, G.P. Reischl, A.O. Lindner, A. Berner, A new electromobility spectrometer for the measurement of aerosol size distributions in the size range from 1 to 1000 nm, J. Aerosol Sci. 22 (3) (1991) 289–296, https://doi.org/10.1016/S0021-8502(05)80007-2.

[28] K.R. May, An 'ultimate' cascade impactor for aerosol assessment, J. Aerosol Sci. 6 (6) (1975), https://doi.org/10.1016/0021-8502(75)90057-9.

[29] P.F. DeCarlo, J.G. Slowik, D.R. Worsnop, P. Davidovits, J.L. Jimenez, Particle morphology and density characterization by combined mobility and aerodynamic diameter measurements. Part 1: theory, Aerosol Sci. Technol. 38 (12) (2004) 1185–1205, https://doi.org/10.1080/027868290903907.

[30] S. Wobrauschek, P. Prost, J. Ingerle, D. Osán, J. Török, Adaption of a TXRF WOBI-module with a low power X-ray tube, in: 18th International Conference on Total Reflection X-ray Fluorescence Analysis and Related Methods (TXRF-2019), 2019.

[31] B. Vekemans, K. Janssens, L. Vincze, F. Adams, P. Van Espen, Analysis of X-ray spectra by iterative least squares (AXIL): new developments, X-Ray Spectrom. 23 (6) (1994) 278–285, https://doi.org/10.1002/xrs.1300230609.

[32] J. Osán, et al., Experimental evaluation of the in-the-field capabilities of total-reflection X-ray fluorescence analysis to trace fine and ultrafine aerosol particles in populated areas, Spectrochim. Acta Part B At. Spectrosc. 167 (May 2020), 105852, https://doi.org/10.1016/j.sab.2020.105852.

[33] F. Gergely, J. Osán, B.K. Szabó, S. Török, Analytical performance of a versatile laboratory microscopic X-ray fluorescence system for metal uptake studies on argillaceous rocks, Spectrochim. Acta Part B At. Spectrosc. 116 (Feb. 2016) 75–84, https://doi.org/10.1016/j.sab.2015.12.007.

[34] A. Bjeoumikhov, N. Langhoff, J. Rabe, R. Wedell, A modular system for XRF and XRD applications consisting of a microfocus X-ray source and different capillary optics, X-Ray Spectrom. 33 (4) (Jul. 2004) 312–316, https://doi.org/10.1002/xrs.733.

[35] A. Bjeoumikhov, N. Langhoff, S. Bjeoumikhova, R. Wedell, Capillary optics for micro x-ray fluorescence analysis, Rev. Sci. Instrum. 76 (6) (Jun. 2005), 063115, https://doi.org/10.1063/1.1938847.

[36] A. Di Cicco, et al., Novel XAFS capabilities at ELETTRA synchrotron light source, J. Phys. Conf. Ser. 190 (1) (2009) 012043, https://doi.org/10.1088/1742-6596/190/1/012043.

[37] P.M. Wrobel, et al., LabVIEW interface with Tango control system for a multi-technique X-ray spectrometry IAEA beamline end-station at Elettra Sincrotrone Trieste, Nucl. Instrum. Meth. Phys. Res. Sect. A Accel. Spectr. Detect. Assoc. Equip. 833 (Oct 2016) 105–109, https://doi.org/10.1016/j.nima.2016.07.030.

[38] A.G. Karydas, et al., An IAEA multi-technique X-ray spectrometry endstation at Elettra Sincrotrone Trieste: benchmarking results and interdisciplinary applications, J. Synchrotron Radiat. 25 (1) (2018) 189–203, https://doi.org/10.1107/S1600577517016332.

[39] B. Ravel, M. Newville, Athena, artemis, hephaestus: data analysis for X-ray absorption spectroscopy using IFEFFIT, J. Synchrotron Radiat. 12 (4) (2005) 537–541, https://doi.org/10.1107/S0909049505012719.

[40] N.C. Burton, S.A. Grinshpun, T. Reponen, Physical collection efficiency of filter materials for bacteria and viruses, Ann. Occup. Hyg. 51 (2) (2007) 143–151, https://doi.org/10.1093/annhyg/mel073.

[41] A. Kiselev, et al., Morphological characterization of soot aerosol particles during LACIS Experiment in November (LExNo), J. Geophys. Res. 115 (D11) (Jun 2010) 13, https://doi.org/10.1029/2009JD012635.

[42] M.L. Eggersdorfer, A.J. Gröhn, C.M. Sorensen, P.H. McMurry, S.E. Pratsinis, Mass-mobility characterization of flame-made ZrO 2 aerosols: primary particle diameter and extent of aggregation, J. Colloid Interface Sci. 387 (1) (2012) 12–23, https://doi.org/10.1016/j.jcis.2012.07.078.

[43] F.E. Huggins, N. Shah, G.P. Huffman, J.D. Robertson, XAFS spectroscopic characterization of elements in combustion ash and fine particulate matter, Fuel Process. Technol. 65, pp (2000) 203–218, https://doi.org/10.1016/S0378-3820(99)00089-2.

[44] I. Swiatkowska, et al., Synchrotron analysis of human organ tissue exposed to implant material, J. Trace Elem. Med. Biol. 46 (Mar. 2018) 128–137, https://doi.org/10.1016/j.jtemb.2017.12.007.

[45] O. Proux, J. Mimault, C. Revenant-Brizard, J.R. Regnard, B. Mevel, Structural evolution of NiAg heterogeneous alloys upon annealing, J. Phys. Condens. Matter 11 (1) (1999) 147–162, https://doi.org/10.1088/0953-8984/11/1/013.

[46] J. Chen, et al., Elucidating the many-body effect and anomalous Pt and Ni core level shifts in X-ray photoelectron spectroscopy of Pt−Ni alloys, J. Phys. Chem. C 124 (2020) 43, https://doi.org/10.1021/acs.jpcc.9b09940.

[47] J.M. Antonini, A.B. Santamaria, N.T. Jenkins, E. Albini, R. Lucchini, Fate of manganese associated with the inhalation of welding fumes: potential neurological effects, NeuroToxicology 27 (3) (1 May 2006) 304–310, https://doi.org/10.1016/j.neuro.2005.09.001. Elsevier.

[48] C. Richardson-Boedler, Metal passivity as mechanism of metal carcinogenesis: Chromium, nickel, iron, copper, cobalt, platinum, molybdenum, Toxicol. Environ. Chem. 89 (1) (1 Jan 2007) 15–70, https://doi.org/10.1080/02772240601008513. Taylor & Francis Group.

[49] K. Salnikow, A. Zhitkovich, Genetic and epigenetic mechanisms in metal carcinogenesis and cocarcinogenesis: nickel, arsenic, and chromium, Chem. Res. Toxicol. 21 (1) (Jan 2008) 28–44, https://doi.org/10.1021/tx700198a. American Chemical Society.

[50] European Commission, 2017/164 of 31 January 2017 Establishing a Fourth List of Indicative Occupational Exposure Limit Values Pursuant to Council Directive 98/

24/EC, and Amending Commission Directives 91/322/EEC, 2000/39/EC and 2009/161/EU, 2017.
[51] Committee for Risk Assessment (RAC), Opinion on Scientific Evaluation of Occupational Exposure Limits for Nickel and Its Compounds, 2018.
[52] D.J. Sivulka, Assessment of respiratory carcinogenicity associated with exposure to metallic nickel: a review, Regul. Toxicol. Pharmacol. 43 (2) (2005) 117–133, https://doi.org/10.1016/j.yrtph.2005.06.014.
[53] "Commission Directive 2006/15/EC of 7 February 2006 establishing a second list of indicative occupational exposure limit values in implementation of Council Directive 98/24/EC and amending Directives 91/322/EEC and 2000/39/EC," 2006.
[54] "Opinion on an EU Binding Occupational Exposure Limit Values (BOELs) for Nickel compounds within the scope of the Carcinogens and Mutagens Directive 2004/37/EC," 2019.
[55] F. Lia, J. Park, J. Tressler, R. Martukanitz, Partitioning of laser energy during directed energy deposition, Addit. Manuf. 18 (Dec. 2017) 31–39, https://doi.org/10.1016/j.addma.2017.08.012.
[56] M. Montani, A.G. Demir, E. Mostaed, M. Vedani, B. Previtali, Processability of pure Zn and pure Fe by SLM for biodegradable metallic implant manufacturing, Rapid Prototyp. J. 23 (3) (2017) 514–523, https://doi.org/10.1108/RPJ-08-2015-0100.
[57] A.G. Demir, L. Monguzzi, B. Previtali, Selective laser melting of pure Zn with high density for biodegradable implant manufacturing, Addit. Manuf. 15 (May 2017) 20–28, https://doi.org/10.1016/j.addma.2017.03.004.
[58] M. Grasso, A.G. Demir, B. Previtali, B.M. Colosimo, In situ monitoring of selective laser melting of zinc powder via infrared imaging of the process plume, Robot. Comput. Integr. Manuf. 49 (2018) 229–239, https://doi.org/10.1016/j.rcim.2017.07.001.
[59] Inconel, Inconel alloy 718, in: Special Metals, 2014.